Pom152 limits NPC dilation in *Schizosaccharomyces pombe*

26/01/2022

Jolijn Govers
5642248
Master's in Molecular and Cellular Life Sciences
Utrecht University

Supervised by
Dr. Martin Beck and dr. Christian Zimmerli
Molecular Sociology, MPI for biophysics, Frankfurt

Examined by
Prof. Dr. Friedrich Förster
Structural Biochemistry, Utrecht University

Abstract

The nuclear pore complex (NPC) bridges the inner and outer nuclear membrane and consists of a nuclear and a cytoplasmic ring that flank an inner ring. The inner ring is surrounded by a luminal ring predicted to be composed of the transmembrane nucleoporin pom152. The NPC is highly dynamic; previous research showed how nuclear envelope tension regulates constriction and dilation of the complex. Which nucleoporins are involved in regulating the NPC diameter has yet to be discovered. During dilation, the luminal pom152 ring changes drastically, forming a ring encircling the membrane closely and potentially regulating the NPC diameter. Here, I used cryo-electron microscopy (cryo-ET) and live cell fluorescence microscopy to investigate the effect of *pom152Δ* on NPC diameter and nuclear volume during hypo-osmotic shock *in cellulo*. My findings show the limiting effect of pom152 on the NPC diameter and imply a nuclear leakage of hypo-osmotically shocked *pom152Δ* cells.

Layman's abstract

In all organisms with a nucleus, this nucleus contains the DNA of a cell. To make use of the information of the DNA, transport between the nucleus and the rest of the cell, named cytosol, is needed. Moreover, this transport must be selective, to assure that molecules that could damage the DNA cannot enter the nucleus and that the DNA does not leave the nucleus.

This transport is facilitated and regulated by the nuclear pore complex (NPC), which is composed of proteins. This complex is situated at the fusion point of the two membranes that separate the nucleus from the cytosol. The NPC consists of three rings: a cytoplasmic ring, an inner ring, and a nuclear ring, that together form a channel spanning the two membranes. The channel is lined with disordered protein domains that facilitate the transport. Surrounding the channel, in the space in between the two membranes a transmembrane nucleoporin encircles the channel. This nucleoporin is named pom152.

The NPC is highly dynamic, causing the channel to constrict and dilate based on the amount of tension that it is subjected to. Under normal conditions, the tension in the nuclear membranes is high, pulling the NPC into a dilated conformation. Upon shrinkage of the nucleus, that can for example be caused by an osmotic shock, the tension decreases, and the NPC is pushed into a constricted conformation. It is so far unknown which nucleoporins are of influence for the maximal dilation and constriction.

Since these conformational changes of proteins are too small to observe with fluorescence microscopy, a technique called electron microscopy is needed to study them. This technique uses electrons to image samples to reach a higher resolution. To assure that the sample does not move during the imaging, it is frozen. Since electrons need to pass through a sample, it has to be thin enough for the electrons to make it through. Most cells are too thick and must be thinned beforehand. So, to allow for protein structures to be determined in their natural environment, a novel method called focused ion beam (FIB)-milling is used, that cuts out thin lamella. Even after FIB-milling, only a limited number of electrons passes through the sample, resulting in a limited signal compared to the noise that will also be generated. Therefore, all proteins of the same type are merged to create an average structure. In addition, an image of the sample under different tilts is acquired, to get the complete 3D information and get an even higher signal compared to the noise. This technique is called tomography.

To study what the effect of pom152 is on the NPC diameter, I induced a hypo-osmotic shock. This shock induces cell and nucleus swelling, hereby also increasing the nuclear membrane tension. After this shock I froze the sample, cut out a thin slice using FIB-milling and imaged the sample using cryo-electron tomography. The average structures I obtained from this showed that in absence of pom152 the NPC is more dilated. In addition, this hypo-osmotic shock caused nuclei of cells without pom152 the nucleus starts to leak. Together these results suggest that pom152 limits the maximal dilation of the NPC. This condition leads reduced cell proliferation.

Introduction

The nuclear pore complex (NPC) is a large macromolecular assembly that bridges the inner and outer nuclear membrane, stabilizing a pore at this fusion point of the nuclear envelope. The complex has a size of approximately 60 MDa in yeast and consists of multiple copies of about 30 distinct types of nucleoporins (nups), forming an approximately 8-fold rotationally symmetric complex. While nups that are rich in phenylalanine-glycine (FG)-repeats are largely disordered, the scaffolding nups provide for the architecture of the NPC. Due to these features, only the scaffolding nups have been addressed structurally. These scaffolding nups assemble into three rings[1]: two outer rings, the nuclear and the cytoplasmic ring (NR and CR) which flank the inner ring (IR) located at the fusion plane of the nuclear membranes. The biochemical composition of the NPC has been shown to vary between species, and even within an organism. However, the composition of the core scaffold of the IR is conserved[2]. The core scaffold is lined with (FG)-rich nups that facilitate size-selective transport[3] and encircled by a transmembrane ring[4].

The luminal part of the transmembrane ring encircling the membrane is predicted to consist of 16 copies of pom152[5,6]. The N-terminus of pom152 is composed of a short disordered cytosolic domain and a single transmembrane α-helix, which together are required for pom152 sorting to the NPC[7]. The C-terminus comprises of the large luminal domain composed of Ig-like domain repeats, that resemble the cell-adhesion mediating cadherins[8]. This luminal domain is presumed to homodimerize in an anti-parallel fashion[6].

The conformation of the NPC is highly dynamic, and a wide range of NPC diameters has been observed[9,10,11], although it is not clear which nucleoporins affect diameter of NPC. Recent research has shown that constriction and dilation of NPCs is dependent on nuclear envelope (NE) tension[12,13]. While the conformation of the NR and CR changes to a minor extent, the IR is subject to more profound conformational changes[12]. The overall conformation of the subunits remains the same, the distance between the subunits decreases substantially. In addition, the conformation of the luminal domain of the transmembrane ring surrounding the IR, that is predicted to be pom152, alters drastically. In a constricted conformation of the NPC this luminal density arches out. In a dilated conformation this density encircles the nuclear envelope, seemingly leaving no room for further pore dilation. We therefore hypothesised that pom152 limits the maximal dilation of the NPC.

To assess the effect of pom152 on the NPC dilation, we used hypo-osmotic conditions to increase the NE tension and induce pore dilation in pom152 knock-out *S. pombe* (*pom152Δ*). The resulting effect on NPC diameter and NE size were assessed by *in cellulo* cryo-electron tomography (ET) and live cell imaging.

Materials and Methods

Culture of *S. pombe*

Frozen *S. pombe* strains stored at -80°C were thawed and plated on YES-agar plates for a maximum of 4 days at 30°C and a maximum of 5 days at room temperature. A single colony was restreaked on a second YES-agar plate, after which another single colony was picked and inoculated overnight shaking at 200 rpm at 30°C. The OD_{600} was kept below 0.8.

Generation of *S. pombe* fluorescently tagged strains

An *S. pombe* strain expressing nup60-mCherry (CZ006; K972 h- nup60-mCherry:Kan) was provided by Christian Zimmerli.

To generate a nup60-mCherry-expressing pom152 knock out strain, a plasmid consisting of nup60-mCherry (pFA6a-mCherry:Kan; GeneArt) was amplified by Phusion High-Fidelity DNA Polymerase-based PCR (NEBioLabs) (forward primer: TCGTTCACGGTTTTGCC; reverse primer: CATGTTTATTCCCAGTTAG). The product was precipitated using 0.3M sodium acetate and 3x sample volume 100% ethanol. The solution was incubated overnight at -20°C, spun down at maximum speed (Eppendorf tabletop centrifuge), washed with 70% ethanol, spun down at max speed for 15 min and dried using a speed-vac concentrator. The final pellet was resuspended in 12 µl H_2O, of which 10 µl was used for transformation.

The pom152KO strain (FY23554 h90 leu1-32 ura4D18 ade6-M210 pom152Δ::kan; NBPR)[14] was transformed with the DNA using an adaption of previously described Lithium Acetate-based methods[15], in which before plating the cells an extra incubation step of 5 hours in 5 ml YES medium was performed at 30°C and 200 rpm. Transformed colonies were selected using selection plates with 100 µg/ml clonat (JenaBioscience). Single colonies were picked and replated on selection plates. Transformed colonies were selected by fluorescence microscopy after overnight incubation in liquid YES medium and stored in 25% v/v Glycerol in YES at -80°C and named CZ019.

Proliferation assay

To check the viability of osmotically shocked WT and pom152KO strains, a proliferation assay was performed by incubating 500 cells of overnight liquid cultures in either YES or ddH_2O for 15 min., after which they were plated, incubated at 30°C and counted 3 days later. The results were statistically analysed in Prism8[16].

Live cell fluorescence microscopy

For preparation of imaging slides, 8-chamber glass bottom slides (Ibidi) were coated with 1 mg/ml Soybean Lectin (Sigma-Aldrich) for 10 min at room temperature. 250 µl of overnight liquid culture with an OD_{600} ranging from 2.5-3.0 was added to the chambers and inoculated for 10 min. A z-stack was acquired pre-osmotic shock, after which medium was removed and replaced by either YES medium or ddH_2O. After 1 minute image acquisition was started with a time interval of 3 min., up to 13 min. after the osmotic shock was induced. The experiments were performed on a Leica Stellaris 5 confocal microscope equipped with a HC PL APO 63x/1.20 water immersion objective with a correction ring, which was set to a Motor Correction Position of 96.8%. The stage was equipped with an incubation chamber that was set to 30°C. Imaging was performed using 1024 x 1024 pixels with a pixel size of 0.18 µm. Z-stacks were acquired with an optical section of 7.1 µm, a pixel size of 0.374 µm and 20 steps. Images were acquired using a dwell time of 0.8625 µs of unidirectional scanning and two rounds of line-averaging. The acquisition of a single z-stack took 2 min. To excite mCherry, a

laser of 587 nm with an intensity of 6.0% was used. The image gain of this channel was set to 50%.

To measure the nuclear area, images were processed in Fiji[16]. First, moving cells were removed from the stacks manually, after which a maximum projection was created, and the resulting image was blurred using the Gaussian Blur function set to 1. The resulting image was binarized using the autothreshold function, upon which merged nuclei were separated digitally using the watershed method, after which the nuclear area was measured by the Analyze Particles plugin, only taking nuclear areas with sizes in between 3 and 9 μm^2 and excluding particles at the edges.

The effect of hypo-OS and *pom152Δ* on nuclear area was statistically evaluated using an ordinary one-way ANOVA test in prism8[16], that calculates statistical differences of means.

Plunge freezing and Focused Ion Beam (FIB)-milling

To prepare the EM-grids, Cu300 R 2/2 (Quantifoil) grids were glow-discharged on both sides and mounted on the Leica EM GP2 plunge freezer with a chamber environment set to ~50% humidity at room temperature.

Cells were plunge frozen by adding 3.5 µl of overnight liquid culture with an OD_{600} of ~0.3 to the mounted grid. To obtain grids with hypo-osmotically shocked cells, the overnight cultures were first spun down for 3 min. at 4000 rpm in an Eppendorf centrifuge and resuspended in ddH_2O prior to addition to the grid. Cells were incubated for ~15 min. at 30°C at 900 rpm on a tabletop shaker (Eppendorf). Next, grids were blotted for 3.5 sec., after which they were immediately plunge frozen in liquid ethane at -184°C and transferred to liquid nitrogen. To allow for shallow angle FIB-milling, the grids were clipped with an autogrid.

FIB-milling of the samples was done as described previously[17], using an Aquilos FIB-SEM (Thermo Fisher). In short, sample grids were first coated with a protective layer of organometallic Pt by means of the gas injection system (GIS-coating) for ~15 sec. Next, the grids were sputter coated with Pt for 20 sec., at a voltage of 1 kV and an Argon gas pressure of 10 Pa. Milling was performed at an angle of 8° in respect to the grid using a stepwise approach, using FIB currents of 1 nA, 0.5 nA, 0.3 nA and 50 pA and aiming for a final thickness of 200 nm.

Automated tomogram acquisition

Tomograms were acquired on a Titan Krios G3i (Thermo Fisher) transmission electron microscope (TEM) equipped with a 300 kV x-field emission gun (FEG) source, a Gatan BioQuantum energy filter and a Gatan K3 camera. Tilt-series (TS) were acquired in dose-fractionation mode using an automated dose-symmetric scheme[18], acquiring tilts from -51° to 51°, using 3° increments and an 8° tilt offset. Tilts were acquired with a target defocus of -2.5 to -4.5 µm, a pixel size of 3.372 Å, and a total dose of 120 – 150 $e/Å^2$.

Image pre-processing, tomogram reconstruction and subtomogram averaging

To acquire NPC diameter measurements, a previously described workflow for tomogram reconstruction and subtomogram averaging was used[12]. In short, tomograms were reconstructed by first removing low-quality tilts such as tilts containing an ice-crystal or a grid bar covering the area of interest. Next, the TS were dose-filtered according to accumulated exposure[19] and extreme value pixels were removed using the IMOD software package[20]. TS alignment was done using an automated script that performed an initial coarse alignment, optimized low-pass filtering and created a final alignment using patch-tracking[12]. The CTF was

estimated with the software package cGTF[21]. 3D CTF correction and tomogram reconstruction were done using NovaCTF[22]. NPCs were manually picked from the reconstructed 4-times binned tomograms, after which particles were extracted and subtomogram averaging (STA) was performed in bin 8 using novaSTA[23], yielding an initial 8-times binned average and a symmetrized average applying 8-fold rotational symmetry.

In case of the pom152KO in control conditions, further averaging was done of 4-times binned tomograms, after which the individual spokes of the NPC were extracted based on previously determined coordinates for further alignment. To assure no false positive subunits were extracted from the dataset, each extracted particle was inspected manually. To get an IR subunit average, a mask covering the entire subcomplex was used, after which another round of IR-focused alignment and averaging was done using a localised mask.

NPC diameter measurements

To measure the diameters of the NPC, particles extracted from 8-times binned tomograms were deconvolved using NovaCTF. For each particle the distance between the membranes was measured manually. For the WT control previous measurements were used.[12] Variations in NPC diameter of the different conditions were subjected to statistical tests in prism 8.

For the pom152KO control the diameter of the central channel was measured as described previously[12], by calculating the position of the center of the channel using 5 to 8 inner ring subunit vectors and deriving the average distance of the subunits from the center. The resulting diameter measurements were compared to previously determined WT NPC control measurements[12].

Results

Pom152 limits maximal dilation of the NPC

To induce NPC dilation, I used a hypo-osmotic (OS) to increase the NE tension. Upon hypo-OS, the cellular and nuclear volume of *S. pombe* increases despite its cell wall, which is a lasting effect[24]. *In cellulo* NPC diameter measurements were obtained using a focused ion beam (FIB)-milling based cryo-electron tomography (cryo-ET) workflow based previously optimized methods[12]. This method consists of inducing a hypo-OS in exponentially growing WT and *pom152Δ S. pombe* cells, adding them on a grid, and subsequently plunge-freezing

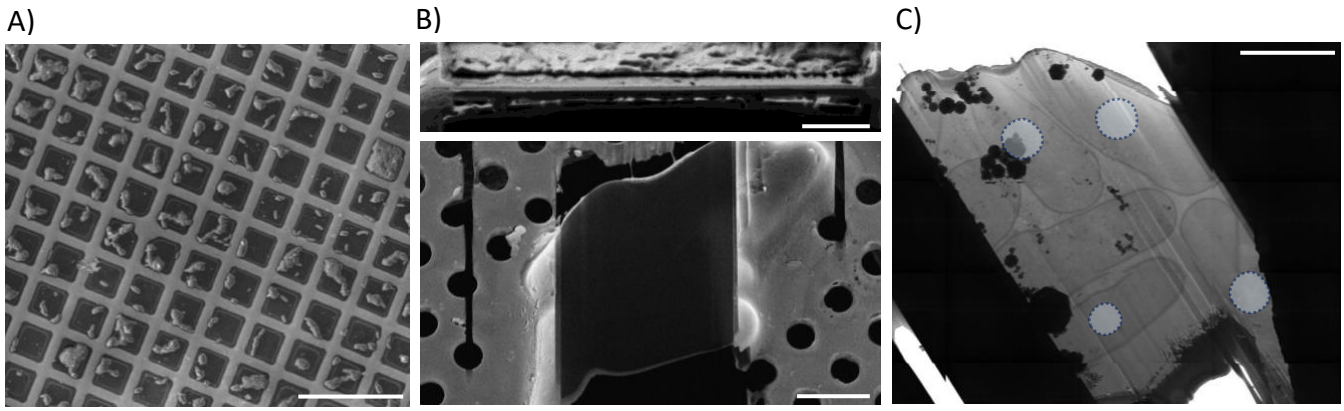

Figure 1: *in cellulo* cryo-electron tomography workflow. A) Cropped image of a scanning electron microscopy (SEM) overview of *S. pombe* grids. The scale bar indicates 300 µm. B) Cropped ion beam (top) and SEM (bottom) image of a polished lamella aimed at a thickness of 200 nm. The scale bar indicates 2 µm and 5 µm respectively. C) Transmission electron microscopy (TEM) image of a lamella at a magnification of 6500x (scale bar 200 nm). The blue circles highlight the nuclei.

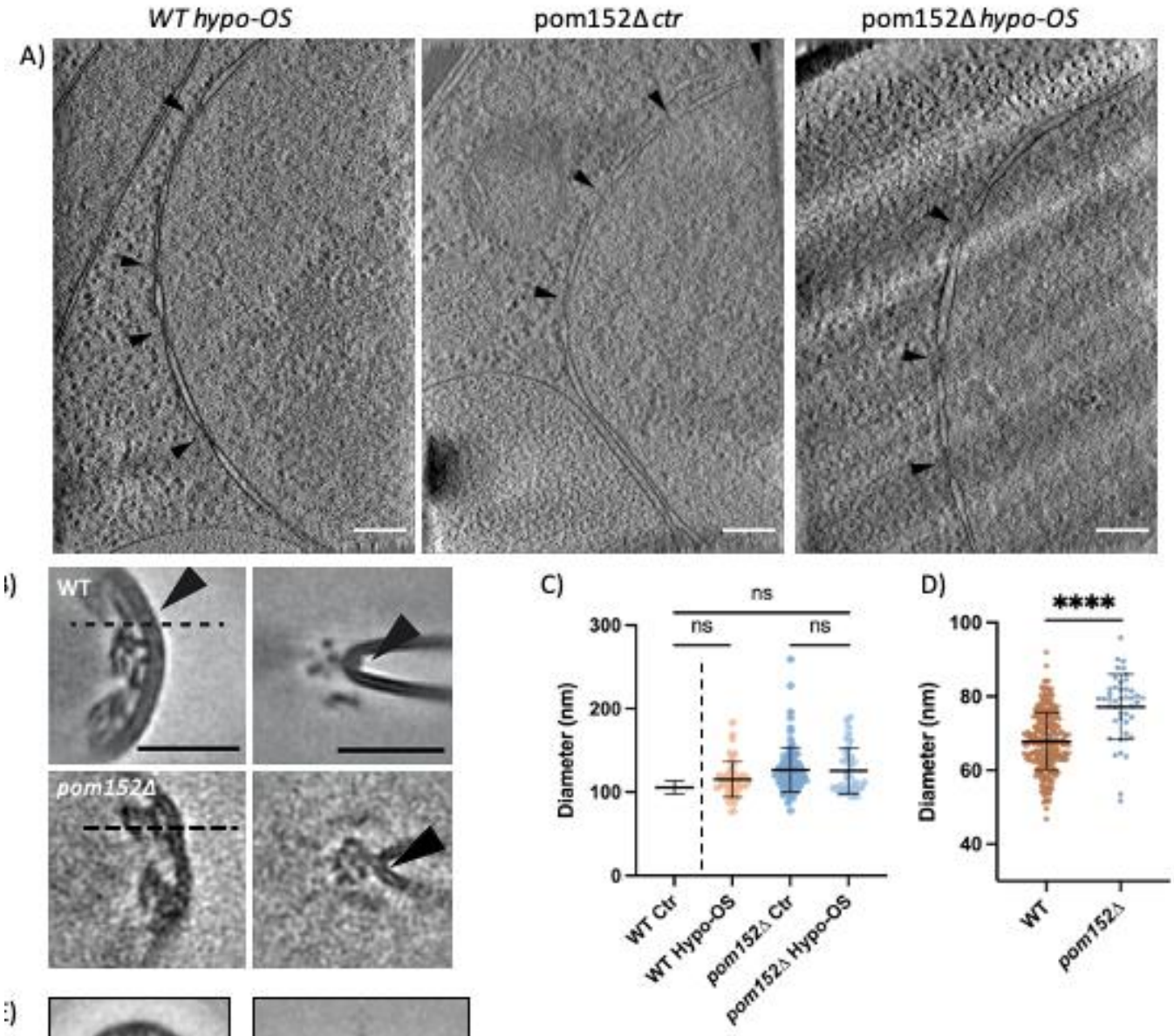

Figure 2: NPC diameter changes upon pom152 knock out under control and hypo-osmotic shock conditions. (A) Slice through representative tomograms of hypo-OS WT and *pom152Δ* in control conditions, and *pom152Δ* in hypo-OS condition. Black arrows indicate NPCs (scale bar 200 nm). (B) Slice through the bin 8 subunit average of WT (top) and *pom152Δ* (bottom). Black arrows point to the location of luminal pom152. The black dotted line indicates the location of the horizontal slice on the right. (C) Membrane-to-membrane diameter measurements as described in methods. For WT control, average measurement, and standard deviation from Zimmerli et al. (2021) were used. One-way ANOVA p* < 0.05. (D) NPC central channel diameter measurements of WT and *pom152Δ* under control conditions. Diameters were derived based on STA determined subunit positions. WT control data was provided by Zimmerli. Student's t-test ****p <0.0001. (E) Slice through 8-fold symmetrized particle average of WT (Zimmerli et al.), WT under hypo-OS (47.5 extracted NPCs), *pom152Δ* (107 extracted NPCs) and *pom152Δ* under hypo-OS (82 extracted NPCs).

the grid (Fig. 1A). In addition, a not-shocked control of each strain was plunge-frozen. To obtain lamellae thin enough for cryo-ET, I FIB-milled the cells to a thickness of 200 nm (Fig.1B). Next, I obtained a lamella overview using TEM, from which I could identify nuclei (Fig. 1C) and determine where the tilt series should be acquired. After acquisition, the tilt series were reconstructed into tomograms (Fig. 2A)

Now I had the tomograms available, I first set out to verify that the luminal ring surrounding the NPC is indeed pom152. To do so, I extracted the different NPC subunits from the tomograms and performed subtomogram averaging (STA). In the WT average, the arrowhead points at the density present in the lumen (Fig. 2B). In the *pom152Δ* strain this density is lacking, indicating that this luminal ring indeed is pom152.

Next, I assessed the differences in diameter between WT and *pom152Δ* under hypo-OS and control conditions by extracting the NPCs and manually measuring the membrane-to-membrane distance for each NPC manually (n = 48 for WT hypo-OS, n = 95 for *pom152Δ*, n = 38 for *pom152Δ* hypo-OS) and plotted together with the WT control the values from Zimmerli et al. (Fig. 2C). These values are also membrane-to-membrane distances, but in this the data was acquired using an automated workflow[12]. The resulting graph indicates a slight increase in NPC diameter upon hypo-OS. Upon *pom152Δ*, the diameter appears to increase in comparison to both WT control and WT hypo-OS, suggesting that the maximal NPC diameter

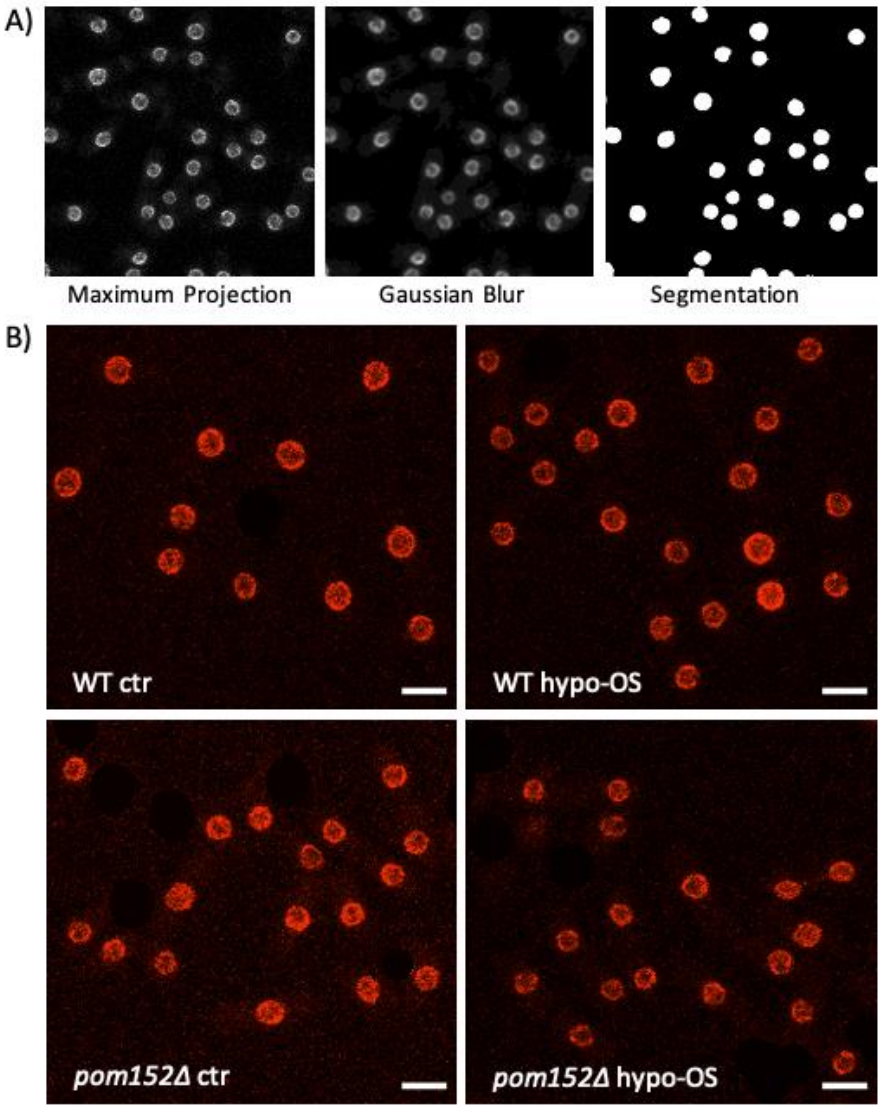

Figure 3: The effect of pom152 on nuclear area and cell proliferation upon hypo-OS. (A) Overview of Z-stack processing steps using ImageJ. First, the Z-stacks are transformed into a 2D image using a maximum projection. Next, a gaussian blur of 1 is used to improve the signal-to-noise ratio. The nuclei are then segmented using the autothreshold function of ImageJ. Areas are calculated using the analyse particle function, filtering out nuclei of 3 > and < 9 to assure that only nuclei are measured. (B) Representative image of a maximum Projection of mCherry-tagged nup60 indicating nuclear area of WT and Pom152KO cells in control and hypo-OS conditions (scale bar 5 µm). (C) Quantification of nuclear areas based on 2D image segmentation (mean ± SD, n = 1775 nuclei). (D-E) Survival assay of WT (D) and *pom152Δ* (E) strains after 15 min. hypo-OS or ctr conditions, normalized to the ctr. (2 biological replicates, 500 plated cells per condition, mean ± SD).

in *pom152Δ* is larger than in WT NPCs. In addition, this data implies that the variation in diameters increases upon *pom152Δ*, resulting in several outliers with an exceptionally high diameter. However, the number of plotted particles is double as well. Upon hypo-OS of *pom152Δ*, the average NPC diameter does not decrease, although the distribution of the data does change considerably. Under control conditions of *pom152Δ* only 15.7% of the NPCs has a diameter smaller than 110 nm, against 31.6% of *pom152Δ* hypo-OS NPCs, suggesting that a relatively large percentage of *pom152Δ* pores has a decreased diameter upon hypo-OS conditions. In addition, the number of pores with a diameter > 150 nm increases from 13.7% to 21.1% upon hypo-OS NPCs. Taken together, these results indicate that *pom152Δ* limits NPC dilation and that the variability in NPC diameters increases upon hypo-OS[12].

To obtain more conclusive NPC diameter measurements, an automated workflow was used to calculate the average distance of each extracted subunit to the centre of the pore. *Pom152Δ* control was the only condition with enough particles to obtain a subunit average with sufficient signal-to-noise ratio to calculate these results. Since this data is obtained using the same method as Zimmerli et al., they are now fully comparable. The resulting graph confirms the earlier observations, showing a significant increase of NPC diameter upon *pom152Δ* (Fig. 2D).

To further compare the differences between diameters of the four conditions, STA was performed on the extracted NPCs. The 8x binned, 8-fold symmetrized averages confirm the previous observations (Fig. 2E), showing a slight increase of WT control compared to WT hypo-OS diameter and a larger *pom152Δ* NPC diameter in comparison to that of the WT. A decrease in membrane-to-membrane diameter of hypo-OS *pom152Δ* is more evident in the averages (Fig. 2C) than the graph (Fig. 2E). Since the smaller diameters are more homogeneous, they result in more coherent average, whereas NPCs with larger diameters are more heterogeneous, resulting in a noisier average. These results indicate that a portion of the *pom152Δ* NPCs constricts upon hypo-OS.

Pom152 affects nuclear area upon hypo-OS

Considering that NE tension affects NPC diameter, it could be that the diameter reduction upon hypo-OS of *pom152Δ* results in reduced NE membrane tension, which has previously been shown to be concomitant with a reduction in nuclear volume[12]. To examine this hypothesis, I measured changes in nuclear area upon hypo-OS in WT and *pom152Δ* by acquiring Z-stacks of NPC-labelling nup60-mCherry with live cell confocal microscopy (Fig. 3A).

A maximum projection of the Z-stacks revealed a large variability in nuclear area within each condition (Fig. 3B). The nuclear areas were segmented, after which the segment

sizes were measured and plotted (Fig. 3C). Since the nuclear volumes are so miscellaneous, these changes are not significant.

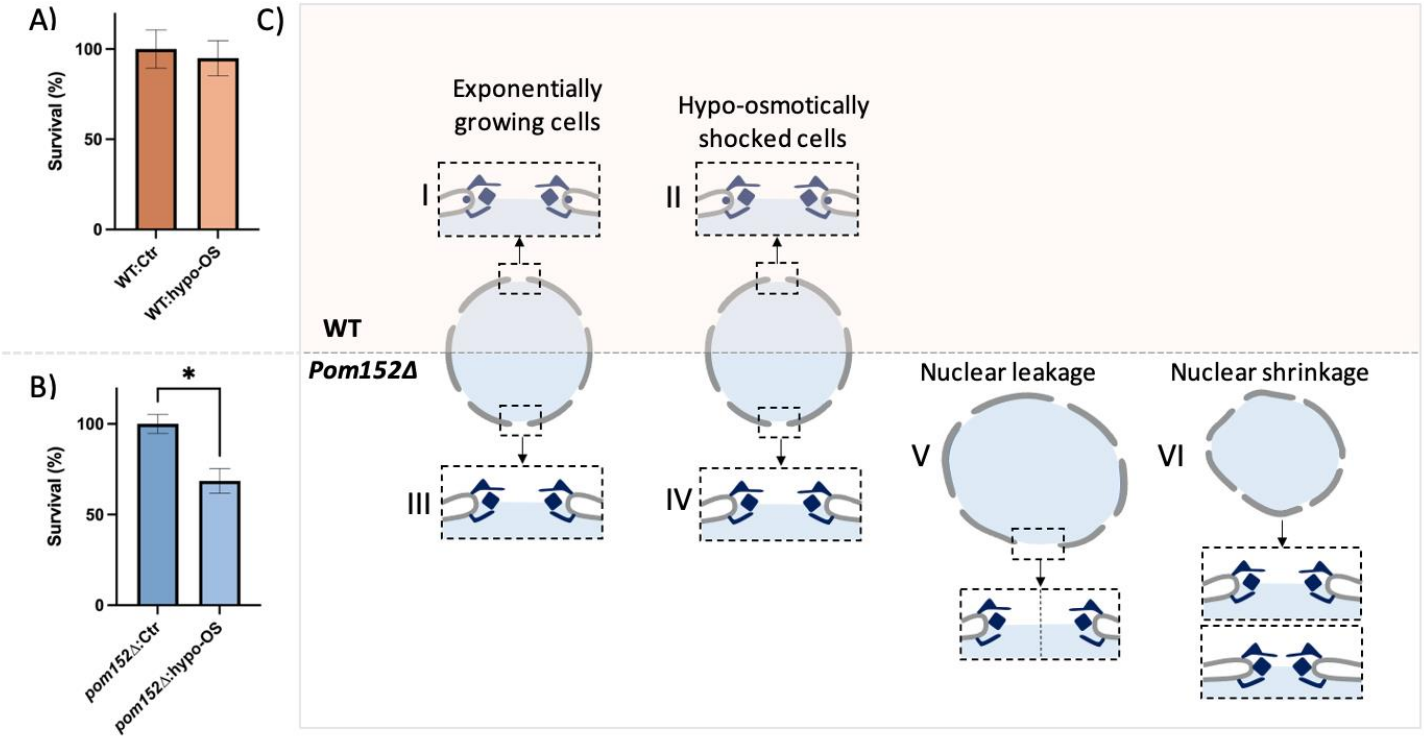

Figure 4: Conceptual model of the effect of pom152 on nuclear area and NPC diameter. (A-B) Survival assay of (A) WT and *pom152Δ* (B) strains after 15 min. hypo-OS or ctr conditions, normalized to the ctr. (2 biological replicates, 500 plated cells per condition, mean ± SD). (C) In exponentially growing WT *S. pombe* cells, NPCs are dilated (I). Hypo-OS has a minor expansion effect, resulting in a similar NPC diameter (II). In exponentially growing *pom152Δ* cells, the NPC diameter is already more dilated than in the WT (III). Upon hypo-OS there is a small nuclear volume increase and the nuclear tension increases (IV). Due to the lack of pom152 some pores will expand to an even larger diameter resulting in nuclear leakage (V), causing nuclear shrinkage (VI). In shrunken nuclei, the NE tension is decreased, leading to NPCs will a smaller diameter. The nuclear leakage sites might not have restored to a smaller diameter yet, resulting in a larger variability in membrane-to-membrane distances.

Upon hypo-OS of the WT, a very small increase in the average nuclear area seems to occur, whereas hypo-OS of *pom152Δ* shows a more profound change in the distribution of nuclear area sizes, implying a decrease in NPC diameter.

Pom152 reduces *S. pombe* hypo-OS survival

Since nuclear leakage could potentially result in chromatin mislocalization to the cytosol and DNA damage, this would likely cause a reduction in cell proliferation[25–27]. I therefore set out to identify the effect of hypo-OS on *pom152Δ* survival. To do so, I performed a proliferation assay by subjecting a similar number of WT and *pom152Δ* cells to hypo-OS and counting the number of colonies that grew after the shock. The percentage of colonies that had survived was normalized to the percentage of colonies that had grown in control conditions. In both WT and *pom152Δ* the percentage of survived cells under control conditions is comparable (94.1 ± 0.10% and 97.6 ± 0.05% respectively). Upon hypo-OS of the WT, there is no significant change in survival rate (94.9 ± 9.8%; Fig. 4B), whereas for *pom152Δ* the survival rate reduces

significantly (68.6 ± 6.8%; Fig. 4C). Taken together these results indicate that pom152 has a profound effect during hypo-OS.

Discussion

This study reveals the location of the pom152 luminal ring in the NPC complex and its limiting effect on NPC diameter, hereby providing a deeper understanding of how the maximum dilation of the NPC is regulated.

The data presented in this research point towards a model in which pom152 is dispensable in exponentially growing *S. pombe* cells, merely resulting in an increased NPC diameter (Fig. 4C). Upon a hypo-OS, the diameter of NPCs lacking pom152 decreases, which could be the result of a decreased nuclear volume resulting from nuclear leakage. NPCs lacking pom152 might be unable to withstand the increased mechanical tension of a hypo-OS, allowing for the pore to dilate even further, resulting in nuclear leakage. Nuclear leakage could result in cellular damage, which would explain the reduced proliferation of *pom152Δ* cells after hypo-OS.

Further research is needed to validate this theory. Firstly, a larger dataset should be acquired *pom152Δ* and WT in hypo-OS conditions so these diameters can be measured in a more reliable, automated fashion. In addition, a larger dataset will provide more insight in the distribution of diameters under these conditions. Secondly, whether nuclear leakage indeed takes place requires further verification. This could for example be identified by studying the leakage of a fluorescent probe conjugated to a nuclear localisation signal (NLS) from the nucleus to the cytoplasm in hypo-OS *pom152Δ* cells using live cell microscopy.

If nuclear leakage indeed takes place, this poses the question what exactly causes it. The leakage could be induced in three different ways: 1) upon hypo-OS of *pom152Δ* the NPC dilates to an even wider conformation, forming a 'super pore'. 2) pom152 lacking NPCs could break, for example by disconnection of the spokes. 3) the NE itself breaks at a different location. Identification of the process underlying nuclear leakage and leak repair could provide new insights into the mechanism by which NE, the NPC, and nuclear integrity are maintained.

In addition, it would be interesting to find out what causes this decrease in cell viability upon nuclear leakage. Previous research has shown that nuclear breakage leads to double-strand DNA breaks in mammalian cells[26]. If the NE leak is large enough for leakage of nuclear proteins and perhaps even chromatin into the cytosol and cytosolic proteins into the nucleus. In this case, it could have a similar effect as the nuclear breakage, which has been shown to induce DNA damage, and could lead to a variability of cellular responses, including cell death[28].

Previous studies predicted the localisation of pom152 in the NPC, suggesting the luminal N-terminal domain of this protein to form a dimerizing transmembrane ring surrounding the NE[4,6]. Previously, the predicted human pom152 homolog GP210 was shown to form a similar transmembrane ring. In GP210 knock out HEK293 cells, this luminal density was lacking[29]. Our results showed that in *pom152Δ* this density was missing as well, demonstrating the similarity of the human and *S. pombe* nups.

While KO of pom152 led to an increase in NPC diameter, KO of GP210 left the diameter unchanged[29]. This could be explained by the differences between GP210 and pom152 conformations in the most dilated NPC conformations structurally predicted so far. Upon dilation in *S. pombe*, pom152 is completely elongated and in close proximity to the NE. Preliminary results from AlphaFold predicitons of pom152 in *S. cerevisiae* confirm this, predicting the protein to form an 8-fold, C2-symmetric ring of 16 copies that forms close interactions within the protein and with the copy in the opposing direction through domain swapping of the Ig-domains. The rings are in an elongated conformation and are close to the membrane.

Upon dilation of the NPC in HEK293 cells, the luminal domain of GP210 remains arched out [29], potentially leaving room for further dilation. The GP210 structure predicted by Obarska and colleagues has 8 copies of GP210 per spoke, adding up to a total of 64 copies. Whether this difference can be attributed to the difference in GP210 number or other diameter limiting nucleoporins remains to be elucidated.

In comparison to *S. pombe*, the Y-complexes of which the nuclear ring is composed are connected in human NPCs, which might restrict the pore dilation under the observed control conditions, potentially limiting the NPC to a smaller diameter than the maximal diameter GP210 would limit the pore to.

There are clues implying that under higher mechanical stress GP210 might be essential. For one, GP210 expression is cell type dependent[30]; it is essential for differentiation of C2C12 myoblasts, and dispensable in HEK293 cells[31,29]. A possible cause for these differences in cell type dependency could be the mechanical tension imposed by the cytoskeleton, which is coupled to the NPC by the LINC complex[32]. Specific cell types are exposed to more drastic changes in mechanical tension than others. Secondly, GP210 is overexpressed in several types of cancer[30,33]; depletion of GP210 has been shown to reduce cell metastasis[34]. Since metastatic cells are subject to a higher degree nuclear deformation due to an increase in migration, this could be a potential explanation as to relation between GP210 overexpression and metastasis. However, recent studies have also showed association of the perinuclear terminus of GP210 to proteins regulating gene expression, which amongst others target genes involved in focal adhesion and cell migration[31,33,34,35]. It could therefore be interesting to study the effect of GP210 on the NPC under increased mechanical tension and dissect the possible mechanisms by which it induces metastasis.

References

1. Beck, M. & Hurt, E. The nuclear pore complex: Understanding its function through structural insight. *Nat. Rev. Mol. Cell Biol.* **18**, 73–89 (2017).
2. Lin, D. H. & Hoelz, A. The structure of the nuclear pore complex (An Update). *Annu. Rev. Biochem.* **88**, 725–783 (2019).
3. Fernandez-Martinez, J. & Rout, M. P. One Ring to Rule them All? Structural and Functional Diversity in the Nuclear Pore Complex. *Trends Biochem. Sci.* 1–13 (2021). doi:10.1016/j.tibs.2021.01.003
4. Yewdell, W. T., Colombi, P., Makhnevych, T. & Lusk, C. P. Lumenal interactions in nuclear pore complex assembly and stability. *Mol. Biol. Cell* **22**, 1375–1388 (2011).
5. Upla, P. *et al.* Molecular Architecture of the Major Membrane Ring Component of the Nuclear Pore Complex. *Structure* **25**, 434–445 (2018).
6. Kim, S. J. *et al.* Integrative structure and functional anatomy of a nuclear pore complex. *Nature* **555**, 475–482 (2018).
7. Brown, J. T., Haraczy, A. J., Wilhelm, C. M. & Belanger, K. D. Characterization of nuclear pore complex targeting domains in Pom152 in Saccharomyces cerevisiae. *Biol. Open* **10**, (2021).
8. Devos, D. *et al.* Simple fold composition and modular architecture of the nuclear pore complex. *Proc. Natl. Acad. Sci. U. S. A.* **103**, 2172–2177 (2006).
9. Mahamid, J. *et al.* Visualizing the molecular sociology at the HeLa cell nuclear periphery. *Science (80-.).* **351**, 969–972 (2016).
10. Allegretti, M. *et al.* In-cell architecture of the nuclear pore and snapshots of its turnover. *Nature* **586**, 796–800 (2020).
11. Stanley, G. J., Fassati, A. & Hoogenboom, B. W. Atomic force microscopy reveals structural variability amongst nuclear pore complexes. *Life Sci. Alliance* **1**, 1–13 (2018).
12. Zimmerli, C. E. *et al.* Nuclear pores dilate and constrict in cellulo. *Science* **9776**, eabd9776 (2021).
13. García-González, A. *et al.* The effect of cell morphology on the permeability of the nuclear envelope to diffusive factors. *Front. Physiol.* **9**, 1–15 (2018).
14. Sugiyama, T., Wanatabe, N., Kitahata, E., Tani, T. & Sugioka-Sugiyama, R. Red5 and three nuclear pore components are essential for efficient suppression of specific mRNAs during vegetative growth of fission yeast. *Nucleic Acids Research* **41**, 6674–6686 (2013).
15. Kumar Rai, S., Atwood-Moore, A. & Levin, H. L. High-frequency lithium acetate transformation of Schizosaccharomyces pombe. *Methods Mol Biol.* 167–177 (2018). doi:10.1007/978-1-4939-7546-4_15
16. Schindelin, J. *et al.* Fiji: An open-source platform for biological-image analysis. *Nat. Methods* **9**, 676–682 (2012).
17. Allegretti, M. *et al.* In-cell architecture of the nuclear pore and snapshots of its turnover. *Nature* **586**, 796–800 (2020).
18. Hagen, W. J. H., Wan, W. & Briggs, J. A. G. Implementation of a cryo-electron tomography tilt-scheme optimized for high resolution subtomogram averaging. *J. Struct. Biol.* **197**, 191–198 (2017).
19. Grant, T. & Grigorieff, N. Measuring the optimal exposure for single particle cryo-EM using a 2.6 Å reconstruction of rotavirus VP6. *Elife* **4**, 1–19 (2015).
20. Kremer, J. R., Mastronarde, D. N. & McIntosh, J. R. Computer visualization of three-dimensional image data using IMOD. *J. Struct. Biol.* **116**, 71–76 (1996).
21. Zhang, K. Gctf: Real-time CTF determination and correction. *J. Struct. Biol.* **193**, 1–12 (2016).
22. Turoňová, B., Schur, F. K. M., Wan, W. & Briggs, J. A. G. Efficient 3D-CTF correction for cryo-electron tomography using NovaCTF improves subtomogram averaging resolution to 3.4 Å. *J. Struct. Biol.* **199**, 187–195 (2017).
23. Turoňová, B. *et al.* In situ structural analysis of SARS-CoV-2 spike reveals flexibility mediated by three hinges. *Science (80-.).* **370**, 203–208 (2020).

24. Nakayama, Y., Yoshimura, K. & Iida, H. Organellar mechanosensitive channels in fission yeast regulate the hypo-osmotic shock response. *Nat. Commun.* **3**, (2012).
25. Denais, C. M. *et al.* Nuclear envelope rupture and repair during cancer cell migration. *Science (80-.).* **352**, 353–358 (2016).
26. Raab, M. *et al.* ESCRT III repairs nuclear envelope ruptures during cell migration to limit DNA damage and cell death. *Science (80-.).* **352**, 359–362 (2016).
27. Irianto, J. *et al.* DNA Damage Follows Repair Factor Depletion and Portends Genome Variation in Cancer Cells after Pore Migration. *Curr. Biol.* **27**, 210–223 (2017).
28. Burhans, W. C. *et al.* Apoptosis-like yeast cell death in response to DNA damage and replication defects. *Mutat. Res. - Fundam. Mol. Mech. Mutagen.* **532**, 227–243 (2003).
29. Mosalaganti, S. *et al.* Artificial intelligence reveals nuclear pore complexity. *bioRxiv* (2021). doi:https://doi.org/10.1101/2021.10.26.465776
30. Ori, A. *et al.* Cell type-specific nuclear pores: A case in point for context-dependent stoichiometry of molecular machines. *Mol. Syst. Biol.* **9**, (2013).
31. Raices, M. *et al.* Nuclear Pores Regulate Muscle Development and Maintenance by Assembling a Localized Mef2C Complex. *Dev. Cell* **41**, 540-554.e7 (2017).
32. Janota, C. S., Calero-Cuenca, F. J. & Gomes, E. R. The role of the cell nucleus in mechanotransduction. *Curr. Opin. Cell Biol.* **63**, 204–211 (2020).
33. Hong, S. H. *et al.* Nucleoporin 210 Serves a Key Scaffold for SMARCB1 in Liver Cancer. *Cancer Res.* **81**, 356–370 (2021).
34. Amin, R. *et al.* Nuclear pore protein NUP210 depletion suppresses metastasis through heterochromatin-mediated disruption of tumor cell mechanical response. *Nat. Commun.* **12**, 1–23 (2021).
35. Gomez-Cavazos, J. S. & Hetzer, M. W. The nucleoporin gp210/Nup210 controls muscle differentiation by regulating nuclear envelope/ER homeostasis. *J. Cell Biol.* **208**, 671–681 (2015).